PHYSICAL REVIEW A VOLUME 40, NUMBER 9 NOVEMBER 1, 1989

Precision mapping of electrostatic fields using interference-narrowed Stark resonances

Dong-Hai Yang,* David Lieberman, Peter van der Straten,
Thomas Bergeman, and Harold Metcalf
Department of Physics, State University of New York at Stony Brook, Stony Brook, New York 11790

(Received 5 December 1988; revised manuscript received 1 June 1989)

We have exploited the interference narrowing of Stark resonances to map electrostatic fields to a previously unattained level of accuracy and spatial resolution. The technique involves stepwise excitation with tightly focused laser light, an atomic beam, and temporal observation of ionization over a region of interference narrowing. Field inhomogeneities as small as 70 ppm have been detected with spatial resolution of 250 μm in three dimensions. The method is used here with rubidium atoms at fields of 3–4 kV/cm, but any alkali-metal atom over a range from a few tens of V/cm to a few tens of kV/cm is appropriate. Ionization rates may be calculated with the WKB quantum-defect method, but the field-mapping results are independent of the theory. Here this mapping technique is used to evaluate two electrode configurations for precision Stark spectroscopy. Field inhomogeneities produced by an electrode with a narrow slit, when properly constructed, are found to be in good agreement with detailed electrostatic calculations. However, discrepancies between field measurements and calculations for a metal mesh over an aperture indicate the presence of unavoidable crinkles of the mesh. We conclude that the slot is the preferred arrangement, and we present calculations that give the field inhomogeneity as a function of the slot size.

I. INTRODUCTION

One area of general physics that has generally not been accessible to precision measurement is the spatial distribution of electrostatic fields in a vacuum. Because numerical solutions of the Laplace equation can often be found to high precision, it is tempting to assume that measurements are unnecessary. However, for complicated configurations of electrodes, particularly in full three-dimensional geometry, such numerical solutions are not trivial. Furthermore, there may be deviations from design geometry caused by machining imperfections, small burrs, bends, etc., so experimental verification can be quite useful at times.

We report here results obtained by mapping electrostatic fields with a new technique using interference narrowing[1–4] of Stark resonances excited by intersecting laser beams. The availability of precision mapping techniques with high resolution in each of three spatial dimensions can make possible a new level of sophistication in the production of electrostatic fields. Since the method[5] involves measurements of ionization rates that change rapidly with electric field, it is not suitable, for example, for plasma diagnostics. Because the narrowing regions are highly localized in field, this mapping technique is normally preceded by a coarse calibration using more conventional methods, such as measurements of Stark shifts or calculations from the assumed geometry. Within these limitations, the method leads to a product of mapping precision and spatial resolution that is several orders of magnitude better than previous methods (see Sec. II). Of course, application to certain problems outside our interest, such as electron lens construction, clearly requires some additional development to combine the electrodes, laser fields, and particle detection.

The specific application of interest to us is the electrostatic fields used in Stark spectroscopy. These experiments often require an aperture in the electrode plates to permit detection of an emitted electron or ion, so there is inevitably some degree of field inhomogeneity. The mapping procedure is used here to evaluate two different standard configurations of apertured electrode plates, namely the mesh-covered aperture and the slotted electrode.

Better methods of producing uniform electric fields make it feasible to access new questions of physics. For example, various experimental tests have very recently been performed in several laboratories[3,6,7] with several different atoms on the WKB quantum-defect (QD) theory of the Stark effect.[8–10] Small discrepancies are being explored, and additional possibilities for exploiting this remarkably successful theory are being pursued. Measurement of either radiative decay or field ionization of a resonance whose energy or width depends sensitively on electric field obviously requires a uniform field over the excitation and decay region. In this regard, there is the possibility of performing a precise, absolute, calibration of electric field. Since the WKB QD theory uses only fundamental atomic constants and very accurately known empirical quantum-defect parameters, theoretical values could be used to establish an absolute electric field calibration to ppm level of accuracy. Conversely, if high-L quantum defects are not accurately known from zero-field data, it may be possible to determine them from accurate measurements of Stark energies and widths of levels for which many L components are intermixed.

Interference narrowing of Stark resonances offers ideal conditions for field-mapping experiments because of the rapid variation of decay rate with field in the regions where narrowing occurs.[1–5] From an experimental curve of decay rate versus field, inhomogeneous fields can be mapped by determining the position dependence of the decay rate in a constant applied field. This is done by steering the two crossed laser beams that stepwise excite the resonance of interest to move the interaction region. Since the only purpose of the lasers is to excite a particular state of interest, the laser linewidth only needs to be narrow enough to resolve nearby levels. We note that this method produces a minimal perturbation of the field that is being measured. The spatial resolution in our field maps, determined by the intersection region of the two laser beams, is about 0.25 mm in each of three dimensions. This is about 50 times smaller than the best of several recent methods used for electric field mapping and measurement (see Sec. II). Furthermore, the measurement precision that we have obtained is about 30 ppm, as compared with values quoted at typically a few percent for previous mapping methods.

After reviewing these previous field-mapping methods in Sec. II, we briefly summarize the theory of interference narrowing in Sec. III. Apparatus and data-acquisition procedures are discussed in Secs. IV and V. In Sec. VI, we discuss our method for solving the Laplace equation for the slotted electrode and for the mesh electrode, and we plot calculated values of an inhomogeneity parameter as a function of the slot dimensions. Results of the mapping measurements for these two geometries are given in Sec. VII. These results indicate that a narrow slot introduces a much smaller degree of field inhomogeneity. A metal mesh can be used over a much larger aperture to obtain more signal at the cost of moderate field inhomogeneity, but crinkles in the mesh introduce unpredictable effects. Prospects for precision electric field calibration using interference narrowing are discussed in Sec. VIII.

II. PREVIOUS FIELD-MAPPING METHODS

Electric field-mapping techniques have a long history and have only recently benefited from the use of lasers. Before the modern era, Langmuir probes[11,12] were used to map the electric potential rather than the field directly. A primary disadvantage of these probes was the substantial perturbation of the field to be measured. In the 1950s the design of vacuum tubes was aided by the use of conducting surfaces in an electrolytic tank[12] to evaluate the fields of complicated geometries, and such methods continue to be of use.[13] More recently, probes have been developed using the electro-optic (Pockels) effect[14,15] and single-mode fiber interferometers.[16] These are never of high accuracy, but are useful in certain situations because they may be free of conducting materials.

Measurement of Stark energy levels or Stark line broadening offers possibility for electric field mapping and calibration both in plasmas and in vacuum. Spectral line broadening methods typically use the width of the Stark manifold of a given Rydberg level, as in helium,[17,18] as a measure of the electric field. This method is clearly limited by other sources of line broadening, such as the Doppler effect and collisions. The actual displacement of Rydberg Stark levels has been used to measure the electric field to about 1% in the cathode fall region of a Ne glow discharge.[19] In that work, the use of intersecting laser beams reduced the region of observation to a volume element $2.5\times2.5\times0.2$ mm^3 (about 1 mm^3). The highest previous spatial resolution to our knowledge employed laser excitation of a molecular Π state. Mixing of lambda doublet components by the field leads to Q-branch emission when P or R are excited, or vice versa. Accuracies of $\pm5\%$ and spatial resolution of 0.1 mm^3 have been reported with BCl (Ref. 20) and NaK (Ref. 21) transitions. This molecular technique has worse spatial resolution than the method reported in the present paper, but it requires only that P, Q, and R emission lines be resolved, and hence is generally applicable if the appropriate molecules are present in sufficient abundance.

III. THEORY

As Refs. 2 and 3 contain rather complete discussions of interference narrowing, the present summary will emphasize the differences between typical cases in Rb and our previous observations in Na. Any alkali-metal Stark state Ψ_j^A may be represented as a linear combination of hydrogen Stark states Ψ_i^{H}:

$$\Psi_j^A=\sum_i c_{ji}\Psi_i^{\mathrm{H}} \ . \tag{1}$$

The alkali-metal ion core potential adds to the purely $1/r$ Coulombic potential and hence couples hydrogenic discrete states with hydrogenic continuum levels Ψ_α^H so that the coupling between an alkali-metal Stark state Ψ_j^A and a continuum level α may be represented as

$$V_{j\alpha}=\sum_i c_{ji}\langle \Psi_i^{\mathrm{H}}|V_{\mathrm{core}}|\Psi_\alpha^H\rangle \ . \tag{2}$$

If there is only one continuum, the ionization rate is then $\Gamma=2\pi|V_{j\alpha}|^2$. When different quasibound Stark states are strongly mixed there may be considerable cancellation among the terms in (2) for one of the eigenstates at some particular field value. If the mixing changes considerably, for example, near an anticrossing, the ionization rate may decrease by several orders of magnitude over a small variation of the field. It is this phenomenon that is exploited in our work.

The ion-core potential is larger in rubidium than in sodium and this has several consequences that affect the occurrence of interference narrowing regions of the type that are of interest here. Most importantly, the discrete-continuum coupling elements are so large that above the saddle-point energy E_{SP} virtually all Stark levels with $M_j=\frac{1}{2}$ and $\frac{3}{2}$ ionize too rapidly to be useful in these experiments. For this reason, Rb Stark energy levels and widths, such as those shown in Fig. 1, can be calculated with a multichannel version of Harmin's WKB QD Stark theory[8-10] utilizing an expansion of inverse tunneling integrals.[10] This method is useful up to slightly above the classical saddle-point energy $E_{\mathrm{SP}}=-2\sqrt{F}$. (See also Ref. 22 for discussions of the Stark effect in Rb and Ref. 23 for comments on the theory of the Stark effect of multichannel systems.) Resonance energies are identified as the zeros of the determinant of a certain matrix Q, where, in the notation of Ref. 10,

$$Q=U^{(2)}\cos\delta-h^F U^{(2)}\sin\delta \ . \tag{3}$$

Here $U^{(2)}$ is a Clebsch-Gordon coefficient representing a transformation between the J,m_J and L,m_L bases, $\cos\delta$ and $\sin\delta$ are diagonal matrices spanning the space of appreciably nonzero quantum defects, $\delta=\pi\mu_L$, where μ_L is the quantum-defect modulo unity ($-\frac{1}{2}<\mu_L<\frac{1}{2}$), and h^F, defined in Ref. 9, is the density-of-states phase matrix for the hydrogen Stark effect. The resonance width, from Ref. 10, is

$$\Gamma=\left.\frac{\mathrm{tr}(\tilde{q}H^F\sin\delta)}{d[\det(Q)]/dE}\right|\Big/_{\det Q=0} . \tag{4}$$

Here $\tilde{q}=Q^{-1}\det(q)$ (q is the adjoint of the matrix of cofactors of Q), and H^F is the hydrogenic density-of-

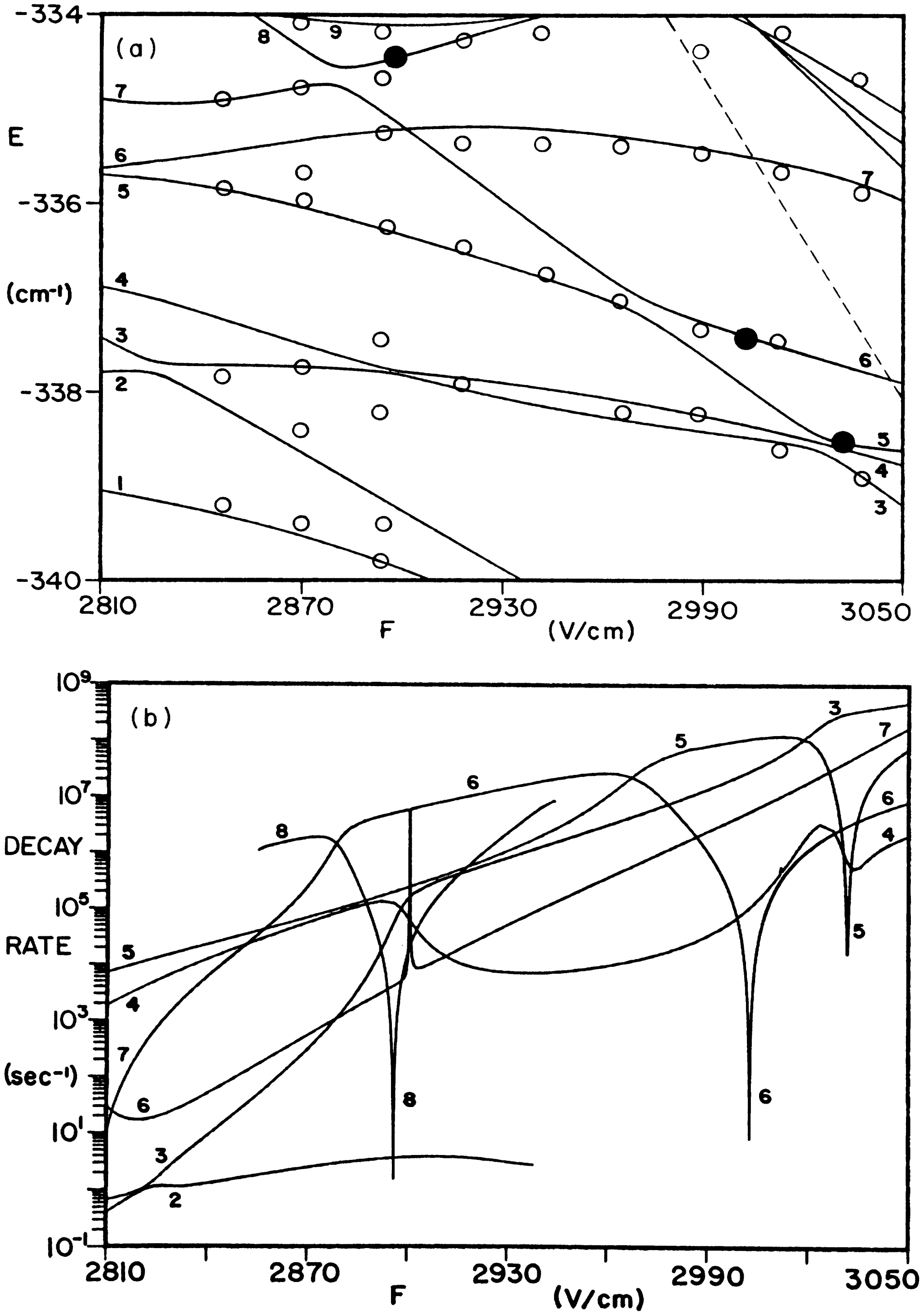

FIG. 1. (a) Energies of rubidium Stark levels showing several narrowing regions (solid circles) and experimental resonance energy measurements (open circles). The saddle point is indicated by a dashed line. (b) Ionization decay rates of the levels shown in (a).

states amplitude matrix. Our computer program evaluates h^F and H^F and then searches for zeros of det(Q) as a function of energy. For Stark maps such as those shown in Fig. 1(a), these zeros are tracked as a function of field with sufficiently small (variable) increments to give an accurate shape for the width function.

All narrowing regions of interest in rubidium have been found just below E_{SP}, as illustrated by the solid circles in Fig. 1(a), which correspond to deep minima in ionization decay rates shown in Fig. 1(b). The actual observed decay rates also include effects of transfer by blackbody radiation and radiative decay, depending on the measurement technique. Frequently, decay minima in rubidium occur near level anticrossings as in Fig. 1. However, this figure also shows that there are anticrossings with no associated narrowing, and conversely we also find narrowings not obviously associated with a level anticrossing, although in such cases the decay-rate minimum is typically not so deep as for the cases in Fig. 1(b). The most narrowly avoided anticrossings [as between curves 2 and 3 in Fig. 1(a)] typically do not exhibit interference narrowing because they occur between states of predominantly different m_L, which decay to orthogonal noninterfering continua.

In contrast, Stark levels in sodium, with its smaller core, preserve the hydrogenlike structure to a much greater degree. There are many regions where $k=2$, 3, or 4 hydrogenic levels cross. In such regions above the saddle point, $k(k-1)/2$ interference narrowings occur.[2,3] $M_L=1$ narrowings that are useful for field mapping may be found even a factor of 2 in field above the saddle point. Thus there are more narrowing regions to choose from in sodium than in rubidium. It is therefore ironic that this phenomenon was first observed in rubidium,[1] but quite characteristic for this atom that they were found very near the saddle-point energy. Of course, field mapping can be performed with a very few narrowing regions if they have the right properties.

A narrowing region useful for electric field mapping can be chosen from possible candidates according to the following criteria: the spectral intensity should be adequate, the range of lifetime values should be suitable for the apparatus, other levels should be far enough away not to bias the data, and of course, the field values should be experimentally accessible. The technique is simplified if there is a negligible energy variation over the narrowing region, so that lasers need not be retuned. We found it convenient to work at the upper end of the range of our voltage source so that the energy levels would be as well resolved as possible. Hence the field region from 3 to 4 kV/cm was searched particularly thoroughly. An ideal case was found at 3455 V/cm and -360 cm^{-1}, unfortunately after most of the mapping data reported below was obtained using the narrowing shown in Fig. 1 at 3003 V/cm, -337.4 cm^{-1}. The former is to be recommended in future uses of rubidium for electric field mapping with this technique. A list of several narrowing regions that we have located between 2.8 and 4.1 kV/cm is given in Table I. Sharper narrowing regions on this list are obviously more suitable when the spatial distribution of field varies less rapidly.

Normally, except for problems with breakdown, etc., field maps can be performed at any field value because only the relative field variation matters. For circumstances where smaller or larger field values are desired, our calculations have shown that there are useful narrowings in Rb, always near the saddle point. These can be found at field values as low as 100 V/cm where they are very abundant, and as high as 25 kV/cm where they are quite sparse. Narrowing regions are rather scarce above 10 kV/cm in Rb because there are fewer level crossings. In Na, clearly defined level crossings with associated regions of line narrowing occur over a very wide range of field values, even quite far above the saddle point and as high as 50 kV/cm.[2,3]

IV. APPARATUS

The apparatus is very similar to that used in our previous experiments,[2,3] but will be briefly described here with emphasis on the changes (see Fig. 2). One major difference is the change from Na to Rb. This change was made in order to be able to study interference narrowing in different atoms and to be able eventually to decelerate the atomic beam with chirped diode lasers. Actually, as noted above, Na would have provided many more regions of interference narrowing.

A thermal Rb beam from a few cm^3 stainless-steel oven at $\sim 200\,^\circ$C with a 0.25-mm-diam hole is directed horizontally (x direction) to an interaction region about 1.1

TABLE I. Useful regions of interference line narrowing in rubidium Stark levels between 2.8 and 4.1 kV/cm. The "nearest-level" columns give the distance in cm^{-1} to the next closest resonance, and its relative intensity on the same scale as used for column 3. All quantities in this table have been obtained from calculations as described in Sec. III.

Field (V/cm)	Energy (cm^{-1})	Relative intensity	Nearest level (cm^{-1})	Intensity	Minimum Γ_{ion} (sec^{-1})	Width at $\Gamma_{\text{ion}}=2\times10^5$ s^{-1} (V/cm)
2896.0	-334.47	2.3	0.31	0.3	2	22
3002.9	-337.40	0.5	0.5	<0.05	8	11
3255.0	-351.88	3.3	1.1	2.6	2×10^4	14
3337.5	-354.46	3.9	0.8	3.3	1.5×10^5	3
3455.6	-360.36	5.2	1.3	<0.05	5×10^2	8
3737.3	-373.67	1.1	1.0	0.3	1.5×10^2	5
4082.9	-391.25	2.0	1.6	1.8	1.4×10^5	3

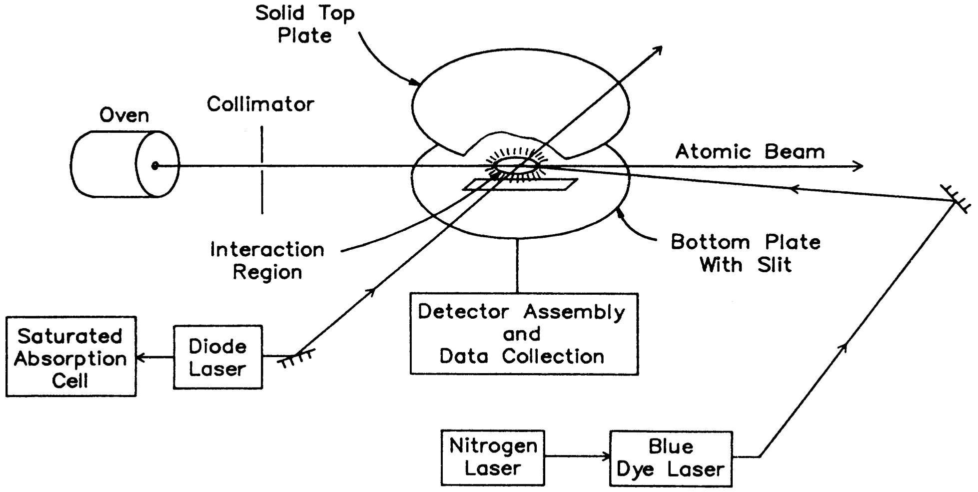

FIG. 2. Overall diagram of apparatus showing laser and atomic beams.

m away. The atoms essentially fill the volume between two oppositely charged, parallel, 3-mm-thick brass plates that produce the z-directed Stark field (vertical). The 75-mm-diam plates are machined and polished to about 25 μm (0.001-in.) flatness, and are separated by four Macor spacers machined and ground to a uniform length of 7.209(5) mm. The degree of plate parallelism attained is shown by the field-mapping results presented in Sec. VII C. In contrast to our earlier work, now the upper plate is smooth and solid, but several different lower ones with a variety of apertures are used to pass the ions resulting from field ionization to a pair of multichannel detector arrays mounted just underneath. The voltage for the field is produced by a Hewlett Packard (HP) 6516A stabilized power supply, and was found to be stable to one part in 10^4 during the data run (about 1 h) by using the atoms themselves as probes. The voltage is measured with a HP 3490A digital voltmeter and a high-voltage probe, but the absolute field calibration is determined from atomic parameters as described below.

Rb atoms in the beam are stepwise excited in the region between the field plates to Stark Rydberg levels by two laser beams. The first beam is from a 780-nm-cw diode laser tuned to excite the $5^2S_{1/2}$ $(F=3)$ level to the $5^2P_{3/2}$ $(F=4)$ level of ^{85}Rb. (This transition is chosen for convenience only: other transitions and ^{87}Rb give the same results.) In order to isolate the diode laser from the effect of stray reflections, its beam passes through a circular polarizer. Since the beam propagates perpendicular to the electric field between the plates, it contains both π and σ components referred to the (vertical) field axis. The second light beam is π polarized (vertical) light from a 486-nm pulsed dye laser (Fig. 2). The horizontal diode laser beam ($\sim$0.4-mm-diam at $1/e^2$ points) crosses the atomic beam about 1.1 m from the oven at nearly a right angle, while the blue dye laser beam ($\sim$0.2-mm-diam at $1/e^2$ points) counterpropagates against the atomic beam. The Doppler width of this blue light from the moving atoms' point of view is comparable to the spectral width of the laser beam. The geometry was chosen to avoid optical pumping by the 780-nm light if it had traveled along the atomic beam, but at the same time to use the intersection of the laser beams to define a small interaction volume that can be moved around to map the field simply by steering the laser beams.

Because the dye-laser excitation near 486 nm selects the Stark states of interest, it must be spectrally narrow, sweepable, and stable. The carefully designed[24] dye laser has a 5-cm-long cavity and two gratings on specially modified mounts to achieve the large free spectral range (3 GHz) that enables easy single-mode operation. Although a single mode is only about 200 MHz wide (Fourier transform limit is 40 MHz), pulse-to-pulse variations resulting from mechanical instabilities limit the effective bandwidth to about 600 MHz $=0.02$ cm^{-1}. This laser is tuned by rotating the Littrow grating, and the required smooth, uniform, repeatable movement is accomplished with a Burleigh Inchworm. We can scan the frequency about 20 cm^{-1} without a mode change. The output of this oscillator is amplified by two dye cells that are saturated by the nitrogen laser pump light to stabilize the output power. This dye-laser system provides sufficient resolution to select Stark states of interest below about 200 cm^{-1} from the zero-field ionization limit.

The Galileo chevron multichannel plates are operated with about 1 kV on each (Fig. 3), and their output is collected on a carefully impedance-matched anode biased at 300 V.[25] The result is a clean pulse easily transmitted on 50-ohm cable and amplified by standard linear pulse amplifiers.[26]

To obtain the average field for a specific configuration of field plates, we made several scans of the laser at slightly different voltages on the field plates. By comparing the observed peak positions with the calculated Stark

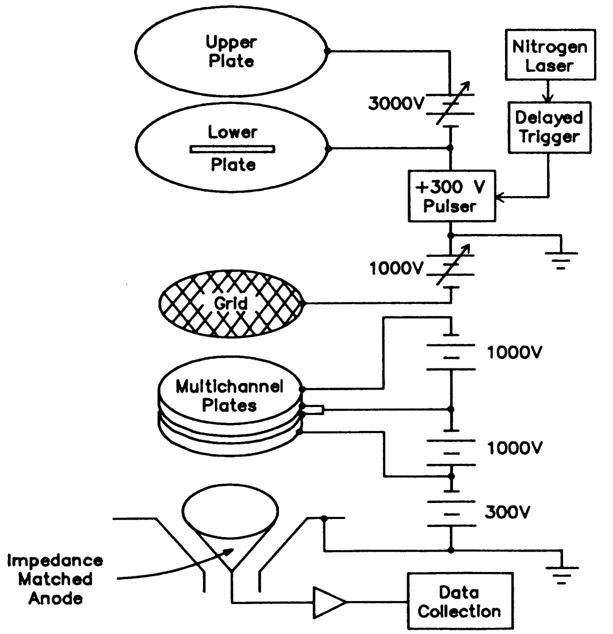

FIG. 3. Block diagram of detector system showing field plates, MCP's, electrodes, and applied voltages. A delayed pulse can be applied to the grid to ionize remaining atoms.

map [see Fig. 1(a)], we can find an approximate relation between the voltage on the plates and the field between the plates. Although this gives us only a modest resolution, it is sufficient to locate the resonances of interest. A subsequent measurement of the lifetime of a particular resonance at different fields yields the field calibration at one point between the plates.

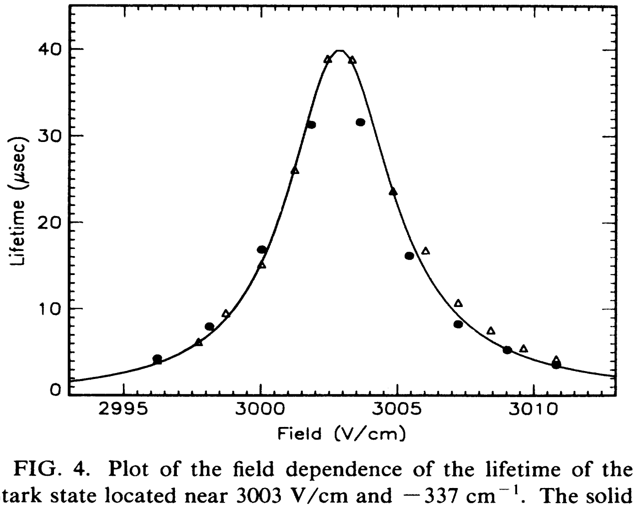

FIG. 4. Plot of the field dependence of the lifetime of the Stark state located near 3003 V/cm and $-337\ \mathrm{cm}^{-1}$. The solid curve is calculated with a $(40\ \mu\mathrm{sec})^{-1}$ decay rate added (chosen to match the peak of the curve) and the points are measured in the absence (triangles) and presence (circles) of a magnetic field. The maximum calculated lifetime of this state against field ionization is ~1 sec.

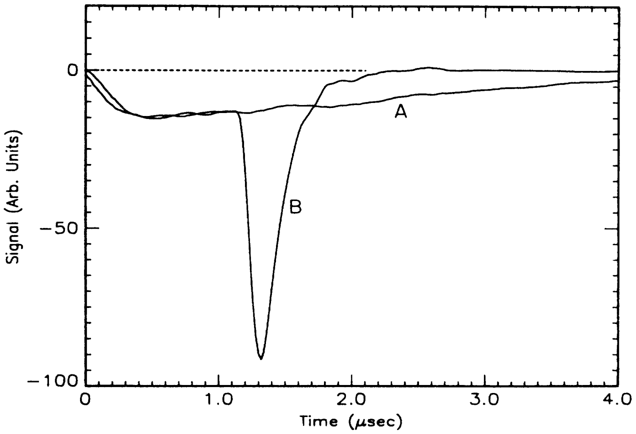

FIG. 5. Ordinary decay signal (*A*) and signal when a pulse was applied to the grid after 1 μsec (*B*).

V. DATA ACQUISITION

A convenient way to exploit interference narrowing for the measurement of fields is to measure the lifetime of a particular Stark resonance at various points in the space between the field plates. To facilitate this we choose a Stark resonance whose lifetime changes rapidly, but not too rapidly, with field over a narrowing region (for an example, see Fig. 4). We then measure its decay time at various positions by moving the intersection region of the laser beams, and use Fig. 4 or its equivalent to determine the field map.

The most obvious way to measure the ionization rate is by observing the time dependence of the ionization signal after the pulsed laser excites the Stark state as shown in Fig. 5. If we use a least-squares method to fit the logarithm of the signal to a straight line, the slope of the line is equal to the decay rate. Figure 6 shows a typical example of such a fit to a decay curve.

For long lifetimes (i.e., small decay rates) there are limitations to this method. First, the small decay rate makes

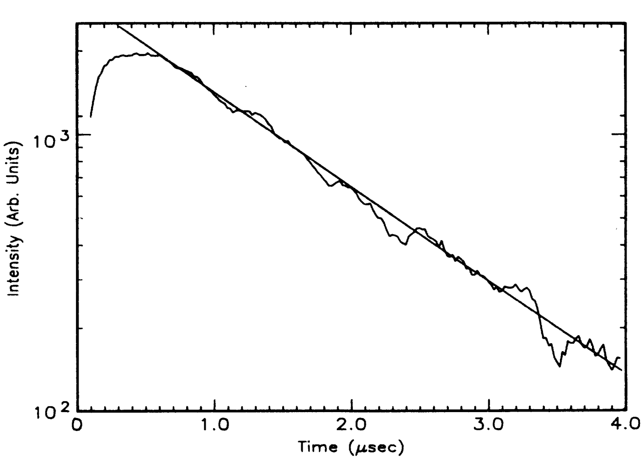

FIG. 6. Semilog plot of a typical decay curve showing characteristic linearity.

the signal weak thereby making it difficult to observe the decay because of the decrease in signal-to-noise ratio. Second, if the lifetime is more than about 30 μsec, corresponding to an average decay length of 1.2 cm, an appreciable fraction of the atoms will leave the detection region before ionizing. Since we have a thermal beam with no velocity selection, it is not easy to account for this effect in our measurements. Third, atoms with long decay lengths are more likely to experience a variation of the necessarily inhomogeneous electrostatic field as they travel between the plates. This can lead to complicated signals because the lifetime is strongly dependent on the field, so that an accurate extraction of the decay rate will be difficult. Fourth, atoms can leave the excited state by processes that do not produce an ion, such as radiative decay or by downward transitions induced by blackbody radiation.

To avoid all these problems, we have used a pulse method to observe long lifetimes. We apply a 300-V pulse to the lower field plate a few μsec after the atoms are excited to the Stark state (see Fig. 3). This causes the field to increase rapidly from a region where the lifetime is fairly long to a region above the saddle point, where the lifetime is very short. The result is a large signal from all excited atoms that survived the interval between the laser pulse and the field pulse. A typical signal is shown in Fig. 5. By integrating the signal over a few μs window with and without the field pulse and comparing the two results, we can determine the decay rate of a state that has a long lifetime in a rather short time. With our apparatus, this method can only be used for lifetimes larger than 0.5 μsec, the time it takes to apply the field pulse to the lower field plate.

There is a range of lifetimes where both the direct decay and the pulse method yield valid results and can be compared. We now consider ways the two methods could give different results. With the decay method, all processes that lead to a decrease of the excited state give a contribution to the measured decay rate. Radiative decay and transfer by blackbody radiation will contribute as well as direct ionization. With the pulse method only ionization processes, either direct or by blackbody radiative transfer to more rapidly ionizing states, give a contribution to the measured decay rate. From the differences between these two methods, we can infer the contributions from nonionizing processes, namely, transfer by blackbody radiation to nonionizing states and radiative deexcitation. In the region of our present observations, the sum of the decay rates from nonionizing processes is typically about 6×10^4 sec^{-1}. A more detailed discussion of these contributions to the total decay rate is planned to be presented in a forthcoming publication. For now we conclude that both methods give a reliable way to determine a decay rate and they should agree within experimental error for lifetimes less than a microsecond.

From knowledge of the field dependence of the lifetime of a particular state (as shown in Fig. 4) and the measured lifetime at various positions, we can produce a map of the electric field. The accuracy of the individual field values is limited only by the combination of signal-to-noise ratio and sharpness of the lifetime dependence on field. As the data below show, we can determine the lifetimes to about 5%, and can choose spectral features whose lifetimes change by a factor of 2 over a field change of less than 0.05%. We are therefore sensitive to field changes as small as ±25 ppm. Although we have made maps with this precision over a limited region, for the plots reported here, the scatter in the data is about 70 ppm.

Most of the data presented below was taken with the Earth's magnetic field canceled by the field from Helmholtz coils around the apparatus. To check for the effect of small magnetic fields on the lifetime measurements, and on the possible ultimate utility of this method for calibrating electric fields, we reversed the current in the coils to double the earth's field at the interaction region. Figure 4 shows that there is no essential difference between the measurements at magnetic field values equal to zero and equal to a few gauss.

VI. CALCULATION OF ELECTROSTATIC POTENTIAL AND FIELD

A. Introduction

To corroborate and extend the experimental maps of electric field, we have computed the electrostatic potential and field for a slotted electrode and for a mesh-covered aperture. The standard method for numerical solution of the Laplace equation is now the finite-element method,[27,28] and several program packages that employ this method are now available.[29,30] We have employed one of these[29] and also our own routines using analytic function expansions in a manner discussed below. The reason for supplementing the standard package, even for two-dimensional calculations, is the precision required and the considerable difference of scale between the slot or mesh structure and the space between the electrodes. This geometry requires several changes in scale in both dimensions in the finite-element method. These could undoubtedly be handled by internal modifications of the program package. However, we would like to point out an alternative approach that is extremely versatile. Within practical limits of the parameters and with appropriate truncation of the problem, the two methods agree very well.

The Schwartz alternating theorem[31–33] for elliptic boundary-value problems states that iterative solution of the Laplace equation in overlapping subdomains converges to a solution for the entire domain of interest. For the first iteration, boundary values for some selected subdomain are provided by a simple model. Calculation of the potential in this subdomain provides estimates for the boundary values for other subdomains lying within. The computed potential in all the subdomains leads eventually to improved values for the potential on the boundaries of this first subdomain, so that one can iterate to convergence. In a recent thesis,[34] it was shown that the rate of convergence generally increases with the degree of overlap. For each subdomain, one is free to select the most convenient method. Although the finite-element method could be used throughout, subdomains of simple, separable geometry can be chosen for the problems at hand, so that analytic function expansions apply.

B. Calculations for an electrode with a slit

We illustrate this method by giving further details for the calculation of the field near a narrow slit in one electrode. The overlapping subregions for the two-dimensional calculation (infinitely long slit) are depicted in Fig. 7. The slit electrode *B* is at ground potential, an electrode below, *A*, provides the Stark field over the observing region, and an electrode above, *C*, accelerates charged particles into a detector or provides a region of nominally null field for studying field penetration. Because the electrodes used were amply large (the diameter to spacing ratio was greater than 10:1), fringing effects were not considered.

According to standard elementary methods,[35,36] the potential Φ in rectangular regions I, II, and III may be represented by a sum of eigenfunction expansions, each of which reproduces given boundary values on one side, or on two symmetric opposite sides. Regions I and III extend sufficiently far horizontally into the regions of uniform field on either side of the slot that the potential on the boundary is represented adequately by $\Delta V/d$, where ΔV is the difference in potential between the plates. Region II overlaps I and III enough for the iteration procedure to converge rapidly. For a better representation of the potential at the corners of the slot, the three-quarter circle regions IV and V (and their mirror images, not shown in Fig. 7) are added. The terms in the analytic function expansion are of the form $(\rho/R)^{2k/3}\sin(2k\phi/3)$, where R is the radius of the subregion. If R is suitably chosen, the potential over the arc is smooth enough to be represented by a modest number of terms. To obtain five-digit accuracy everywhere, typically we have used 150 terms.

At the start of the iteration procedure, the potential is assumed to be zero within the slot and linear on either side. This provides boundary conditions for region II, whose solution gives improved estimates for the potential across the slot apertures, which are part of the boundary of regions I and III. From the calculated potential in regions I, II, and III, boundary values for regions IV and V are obtained. Iteration then proceeds at the sequence II$\rightarrow$III$\rightarrow$I$\rightarrow$IV$\rightarrow$V$\rightarrow$II, etc., until the potential V_α at some critical point, such as the center of the slot, changes by a negligible fraction. After ten iterations, successive increments in V_α are typically less than one part in 10^6. Over the experimentally accessible region, the convergence is even more complete.

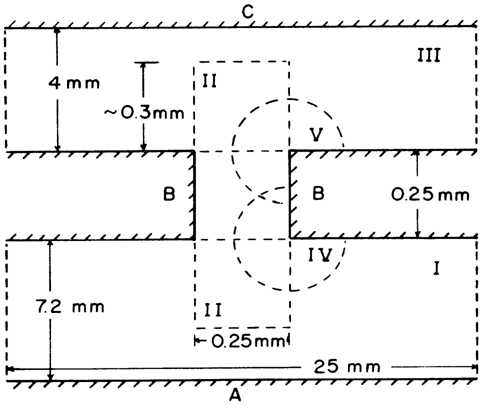

FIG. 7. Schematic diagram of the subdomains used for the calculation of the electrostatic field for a slotted electrode by the Schwartz alternating method. To show the subdomains clearly, the slot and the electrode spacings are drawn to different scales.

Figures 8 and 9 show the potential contours (solid lines) and electric field lines (dashed lines) for the slotted electrode problem. For Fig. 8, the field on the top side is nominally zero, while for Fig. 9, the electric field values on either side are equal. Figure 10 shows contours of the difference between the two cases with an increment $\frac{1}{50}$ of that used in Figs. 8 and 9.

Our calculations with the POISSON/SUPERFISH group codes[29] produced results that agree with those obtained as described above within limitations of these codes. The maximum number of grid points with the version available to us was 10 000 (each grid point involves several coefficients). In view of the restrictions on multiple changes of mesh size, we truncated the geometry to a square region 2.5 mm on a side, with a 0.25-mm-wide aperture in a 0.25-mm-thick plate. Near the aperture, the contour lines were essentially identical with the results shown in Figs. 8, 9, and 10. The field for the actual experimental geometry could undoubtedly be obtained with this program package by application of the Schwartz alternating procedure, or by internal modification of the codes.

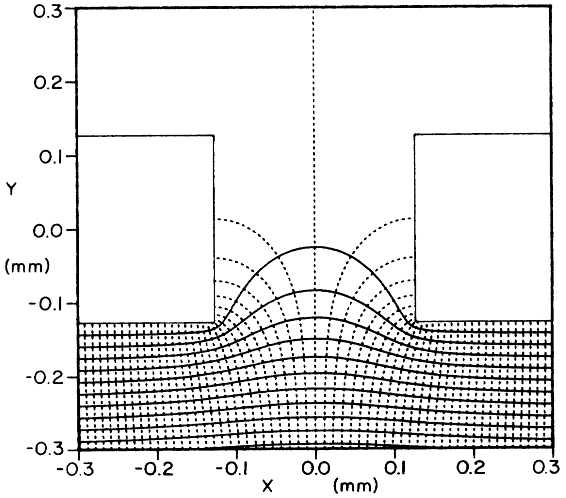

FIG. 8. Equipotential contours (solid lines) and electrostatic field lines (dashed) calculated by the Schwartz alternating method for a slotted electrode plate. The electric field is nominally 3000 V/cm below the slot and zero above, as established by electrodes 7 mm distant on either side. The interval between contours is 5 V.

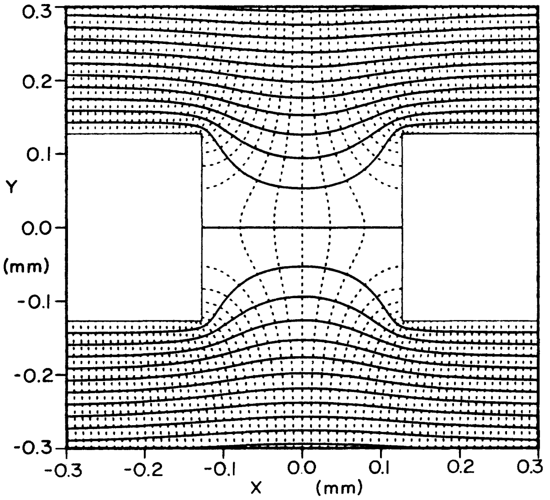

FIG. 9. Equipotential contours (solid lines) and electrostatic field lines (dashed) calculated for a slotted electrode plate. The electric field is nominally 3000 V/cm above as well as below the slot, as established by electrodes 7 mm distant on either side. The interval between contours is 5 V.

C. Field inhomogeneity parameters for a slit electrode

We now exploit results obtained as described in Sec. VI B to represent the field inhomogeneity over the observation region to lowest order. The exact numerical results for the potential are fitted to a two-term expansion

$$\Phi=\tilde{E}_0 y+E_1\cos(\alpha x)\exp[\alpha(y-D/2)] \ , \qquad (5)$$

where D is the plate spacing, x is the transverse distance from the slot center, and y is the vertical distance from the unslotted plate. (The accuracy of this representation decreases sharply close to the slot.) Each term in (5) satisfies the Laplace equation, but with undetermined boundary conditions. The primary interest is in the region directly below the slot ($x=0$) and midway between the plates. We therefore write the electric field

$$E(x=0,y)=E_y=-\frac{\partial\Phi}{\partial y}=-\tilde{E}_0[1+\beta\exp(\bar{\alpha}\bar{y})] \ , \qquad (6)$$

where $\bar{y}=(y-D/2)/D$ is the distance from the midpoint divided by the plate spacing, $\bar{\alpha}=\alpha/D$, and $\beta=E_1\alpha/\tilde{E}_0$. Values for $\tilde{E}_0$, β, and $\bar{\alpha}$ are obtained from calculated values of the potential at $\bar{y}=0$ and $\pm\frac{1}{5}$. Because of the slot, $\tilde{E}_0$ is not equal to $E_0=V_0/D$, where V_0 is the applied voltage, as will be evident from figures presented in Sec. VII. However, because correction terms for $\tilde{E}_0$ are frequently less than the measuring uncertainties of D, we concentrate here on the second term in (5) and (6).

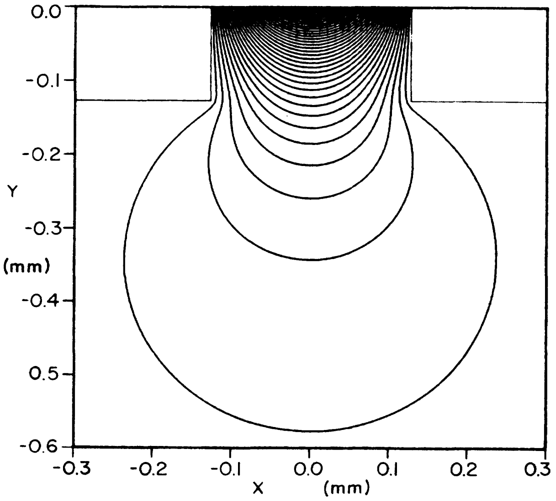

FIG. 10. Contours of the potential difference between the results for Figs. 8 and 9. The interval between the contours is 0.1 V.

From many fittings of calculated potential distributions to (5) and (6), we find that $\bar{\alpha}$ varies only slightly with the scaled thickness of the slotted plate, T/D (for T/D values from 0.01 to 0.05, $\bar{\alpha}$ varies linearly from 6.8 up to only 7.5), and negligibly with the scaled slot width W/D. This range of values of $\bar{\alpha}$ implies that the field inhomogeneity term increases by a factor of e over about one-seventh the plate spacing. The β values vary more drastically and are represented in Fig. 11 in ppm units. In

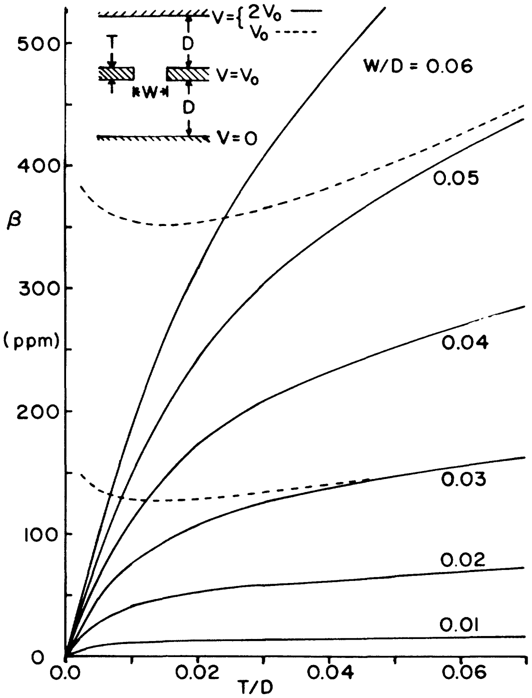

FIG. 11. A representation of the field inhomogeneity due to a slit in an electrode plate. The coefficient β (in ppm) of the inhomogeneity term in Eq. (11) is plotted as a function of the electrode thickness T divided by the electrode spacing D for various values of the slit width W divided by D. Solid lines are for equal field strengths on either side of the slit, dashed lines represent results when the field is nominally zero on the opposite side.

these calculations, the observation region was assumed to be below the slot (inset, Fig. 11) and the spacings on either side of the slotted plate were taken to be the same (the results do not depend critically on the geometry on the opposite side of the slot). For the solid lines in Fig. 11, the field on the opposite side of the slotted plate is equal to the field on the observation side, while for the two dashed lines, the field on the opposite side is nominally zero. The inhomogeneity term of course tends to zero with the slotted-plate thickness if the field is nominally the same on either side of the slot.

From Fig. 11, it is noted that if the electric field is the same on either side of the slot, the inhomogeneity term increases rapidly with T/D up to one or two times the scaled width W/D, and then is less sensitive to further increases in the thickness. The inhomogeneity term is a sharp function of the slot width W. For parameters $T=W=0.25$ mm, as in the present apparatus, and for $D=1$ cm, β is about 80 ppm. Two mm from the slot ($2/\bar{\alpha}$ above the midpoint), the inhomogeneity term in (5) is e^2 times this, or about 580 ppm. Signal amplitudes will normally increase with slot width. Figure 11 therefore helps to determine the trade off between signal amplitude and field homogeneity. In addition, the parameters defined in (5) and (6) and plotted in Fig. 11 can be used to derive limits on the laser-beam diameter consistent with a desired degree of field uniformity over the excitation region.

D. Calculations for a mesh-covered aperture

The mesh problem is considerably more complicated because it does not reduce to two dimensions. We are aware of only one published detailed study of the electrostatic fields associated with a mesh.[37] (The specific configuration of interest here is not considered.) Although there exist commercial computer program packages[30] that are capable of solving the Laplace equation in three dimensions, the number of computational grid elements required for each physical mesh element makes a straightforward approach impractical. For purposes of comparison with the experimental data below, it will suffice to present results obtained from an array of infinitely long strips. Calculations with infinite arrays of strips and meshes in two and three dimensions indicate that the two-dimensional problem is an adequate approximation.

We therefore consider (model A) an array of infinitely long strips parallel with and covering a long aperture in a solid conducting plate with the same dimension used in the experiment (6-mm-wide aperture and 3-mm-thick plate). The strips have the same thickness (7 μm), period (25 μm), and transparency (73%) as the actual mesh. The field is produced by a charged electrode on one side; the mesh itself and an electrode on the other side are at ground potential. The results can be characterized in terms of an average correction potential V_{ci} over each mesh period. (For a solid metal electrode, all V_{ci} would be zero.) The correction potential falls off slightly from the center to the edge because of the effect of the plate thickness.

To estimate the discrepancies resulting from the assumption of infinitely long strips rather than the actual orthogonal mesh wires, we consider an infinite array of strips in two dimensions (model B) and a three-dimensional array of orthogonal wires (model C). Each of these infinite arrays can be solved by considering a single-unit cell with Neumann boundary conditions (e.g., $\partial\Phi/\partial x=0$) on the vertical boundary surfaces. The results of these calculations may be expressed in terms of average correction potentials V_c over the mesh surfaces, as with model A. If the percent transparency is kept constant, the correction potential values for models B and C agree to within 10%, and also agree to within a few percent of the average potential over the central apertures in the model A. Finally, we define model D to consist of electrode strips i each with the width of the mesh period and a potential equal to V_{ci} from model A. We verify that these V_{ci} values over mesh apertures reproduce the spatial distribution of the field obtained from model A to within a few percent, provided one is at least two mesh spacings from the mesh surface so that the periodic variation of the field from the individual wires is negligible. Hence we accept the field values obtained from the finite array of infinite strips as an adequate approximation. Results of this calculation are presented along with experimental data in Sec. VII B.

VII. MEASUREMENTS

A. Introduction

The primary goal of field-mapping measurements that we have performed to date has been to evaluate electrode configurations used for detecting atomic ionization in an electric field. Traditionally, the most common arrangement has been a wire mesh placed over an aperture. Often a sufficiently uniform field is obtained by this means. However, as the measurements reported below indicate, it is very difficult to construct a mesh surface that is extremely flat. An alternative configuration is a long slit parallel to the atomic beam. This yields a smaller signal, but provides a much more homogeneous electric field. The results obtained by our mapping technique in several cases show the effects of deviations from the intended geometry. When these deviations are small, the mapping corroborates electrostatic field calculations for the design geometry.

B. Field mapping with a mesh-covered aperture

Wire mesh electrodes are used in many situations where a uniform electric field is needed behind an aperture that must be highly transparent to charged particles. It is often assumed that at a few mesh spacings from the mesh surface, the field assumes its nominal value $\Delta V/d$ for two electrodes with potential difference ΔV separated by a distance d. Calculations described in Sec. VI D contradict this assumption. The periodic variation of the electrostatic field does damp out rapidly, but if the field on the two sides of the mesh is not the same, the stronger field penetrates the mesh such that δV, the difference between the average potential in the mesh plane and the potential on the surface of the wires is not zero. The field correction term $\delta V/d$ is significant over distances on the scale of the entire mesh aperture. Hence there are spatial variations in the field at the edge of the mesh aperture, and the correction term extends all the way to the planar electrode. If the electrode spacing is 400 times the mesh period and if the field on one side of the mesh is nominally zero, the field correction term at the planar electrode is slightly more than 3000 ppm.

In principle, both the short-range periodic effect and the long-range field correction term $\delta V/d$ are measurable with our interference narrowing method of field mapping. However, with the fine meshes of interest here it is not possible to probe sufficiently close to the mesh surface to detect the periodic variation of the field. An absolute calibration is difficult because of measurement uncertainties in the electrode spacing, contact potentials, and possible imprecision in WKB QD Stark theory (see Sec. VIII). Nevertheless, the spatial variation of the field due to the penetration is easily observable. However, we have found that ripples or crinkles in the mesh surface produce effects that are comparable to or larger than the field penetration term, as results presented below will show.

To maximize our sensitivity to the mesh structure, we make the field on the opposite side of the observation region nominally zero by covering both sides of a 6-mm-wide by 25-mm-long slot in a 3-mm-thick plate with meshes in electrical contact with the plate. An electroformed nickel mesh[38] of period 0.25 mm (100 lines/in.) and thickness 5–8 μm having a transparency of 73% is used. We have examined the mesh with an electron microscope and found a regular pattern of square holes with some small irregularities near the edges of the holes. A thin mesh such as this minimizes the effect of the mesh thickness but is rather fragile. After testing several methods for fastening the mesh over the holes in the brass electrode plates, we found that gluing was the most successful.[39] By carefully stretching the mesh and holding it on the electrode, we managed to mount three pairs of meshes that did not appear to be substantially crinkled or deformed.

The large aperture of the slot allows us to scan the field between the plates in three directions by steering the laser beams. Results of field-mapping measurements along a vertical line at the center of three different mesh-covered apertures are shown in Fig. 12 together with the corresponding theoretical field distribution (solid line). Because the deviations from theory are quite significant, we have adjusted each of the experimental data sets to give a zero deviation very near the solid electrode, although the theory indicates a 0.3% (9-V/cm) correction at this point. Therefore the zero of the scale differs for each experimental data set and for the theory. It is clear that for two of the three meshes, the field increases closer to the mesh, in contradiction with theory and with physical intuition. For the mesh that does exhibit a deviation of the correct sign, the magnitude of the change between the flat plate and the mesh is about twice the calculated value.

The nature of the mesh imperfections is indicated more clearly by horizontal scans of the field. For one of the meshes with a positive deviation in Fig. 12, field scans along the beam axis (centered in the transverse direction) at various vertical positions are shown in Fig. 13. Near the solid plate, the inhomogeneities are very small. The substantial variation of the field near the mesh suggests that there are ripples or crinkles in the mesh. Approximate calculations indicated that 30-μm ripples are enough to produce the observed irregularities. Examina-

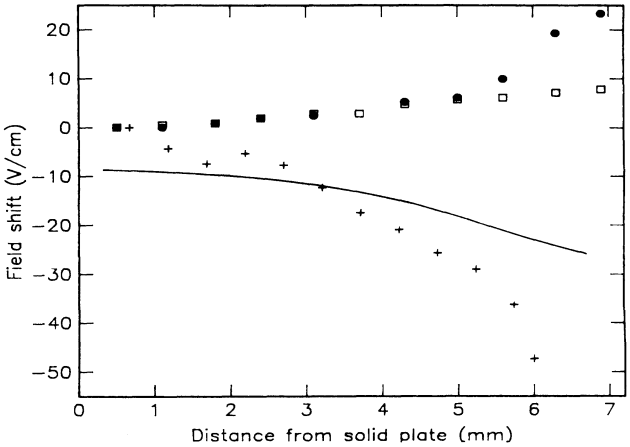

FIG. 12. Electric field variation along a vertical line between electrodes separated by 7.2 mm, at the center of a 6.4-mm by 25-mm aperture in one electrode, both sides of which are covered with electroformed mesh with 100 lines/in. (period 0.25 mm). Calculated values are given by the solid line. The circles, squares, and crosses, for three different meshes, denote measured values, shifted so that each data set is zero at the solid plate. Hence for the experimental data, only the relative field variation over the vertical line is significant. The deviations from theory are associated with crinkles in the mesh.

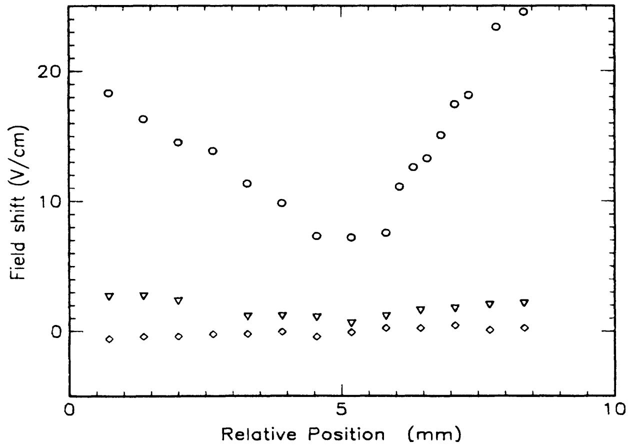

FIG. 13. Field distribution in the horizontal direction along the atomic beam for the mesh denoted by solid circles in Fig. 12. The diamonds, triangles, and circles refer to data obtained, 0.5, 3.1, and 6.3 mm, respectively, from the flat electrode, as compared with the electrode spacing of 7.2 mm. Since the absolute field shift cannot be determined, the vertical scale is adjusted so that the shift is zero at the center of the first scan (0.5 mm from the solid plate).

tion of the mesh by viewing reflections of the overhead fluorescent lights revealed slight ripples persisting despite extreme precautions taken in gluing the mesh to the electrode surface. The utility and sensitivity of the field-mapping technique is apparent.

C. Field maps for a slit electrode plate

A long thin slit in the electrode plates parallel to the atomic beam produces maximal field uniformity along the decay path. It also happens that the field variation even in the transverse direction directly under the slit (the region from which ejected particles are detectable) can be reduced to a negligible value because the slit can be much narrower than the electrode spacing. Of course, the signal is less than with a mesh over a wide aperture. The slits we have used were about 25 mm long and typically 250 μm wide, carefully aligned parallel to the atomic beam.[3,25] The excitation region was just under the middle of this slit. In our report of studies on the interference narrowing phenomenon in Na,[3] a slit of this design was used, and some preliminary field inhomogeneity measurements were included.

When the field distribution produced with this electrode was mapped more carefully with Rb, the vertical and longitudinal variation shown by the solid triangles in Figs. 14(a) and 14(b), respectively, was obtained. The field was found to *increase* as the interaction region was moved closer to the slit [Fig. 14(a)]. This is opposite to what is calculated from elementary electrostatics. Also [Fig. 14(b)], the field was maximum at the slit center and decreased toward either end. These observations led us to perform a careful examination of the slit that revealed a very small lip along both of its edges that had been left by the machining process.

We therefore lapped and polished the brass disk to remove this lip, and repeated the measurements. The open circles in Figs. 14(a) and 14(b) show the field variation in the vertical and longitudinal directions for the slit after lapping, while the solid line [Fig. 14(a)] gives the calculated field distribution. Figure 14(a) shows that the field is most uniform near the solid plate (as expected), and retains this uniformity for more than half the distance to the slit. Figure 14(b) shows that the field variation along the slit after lapping is dominated by the nonparallelness of the plates. There is a field change of about 2 parts in 3000 along a 1.5-cm horizontal path, corresponding to about a 25-μm (0.001-in.) variation in the size of the four spacers on a ~75-mm circle.

Having obtained a good approximation to the ideal slit geometry, we now present additional measurements and calculations as a function of slit width and of the magnitude of the electric field on the opposite side of the electrode (field penetration). Figure 15 shows the results of measurements in the vertical direction that were performed on two new slits of width 250 μm (0.010 in.) and 500 μm (0.020 in.) that were made by electron beam machining and therefore had no mechanical artifacts. To try to detect the effect of the accelerating voltage on the opposite side of the plate, a charged grid electrode was placed between the slitted electrode and the multichannel plate, to provide fields of 0, 500, and 1000 V/cm with both slit widths (see Fig. 3). For the narrower slit, the calculations all fall within the width of the solid line in Fig. 15, while for the wider slit there is a small difference. In either case, the effect of the applied grid voltage is always less than the 0.2-V/cm rms scatter in the experimental data. The correction relative to the nominal value very near the surface of the plane electrode, about 0.2 V/cm, is obtained from the electrostatic field calculations, and the scale for the experimental points is adjusted to agree, since the absolute field strength is not determined. The experimental points in Fig. 15 agree with calculations to about 1 part in 10^4 except for one point just 0.6 mm from the 0.5-mm slit where the field inhomogeneity over the 0.25-mm-diam interaction region is significant.

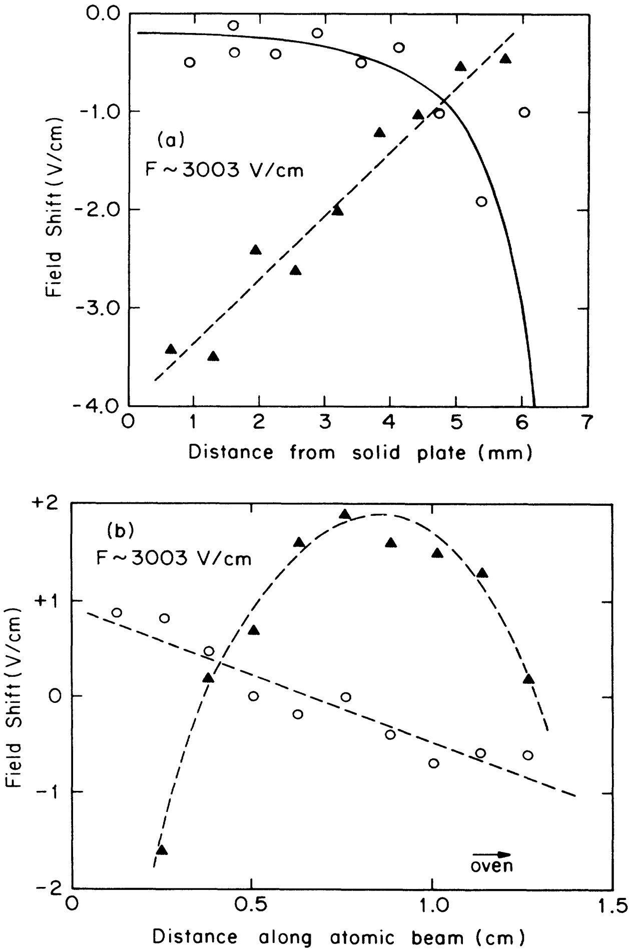

FIG. 14. (a) Electric field variation along a vertical line at the center of a 0.25-mm-wide slit machined in one of two electrodes separated by 7.2 mm before (triangles) and after (circles) lapping to flatness. The bold curved line is the calculated field, while the straight line is merely sketched. (b) Field maps along a horizontal line of the same slit. Triangles and circles have the same significance as in (a). The lines have been merely sketched to guide the eye. Experimental scales have been vertically adjusted for convenience.

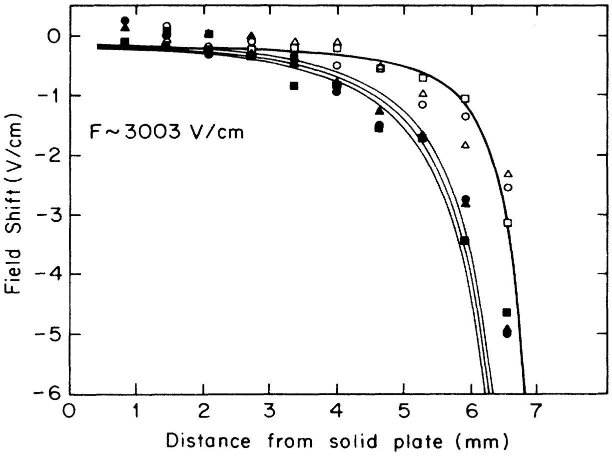

FIG. 15. Vertical field map and calculated fields for the slit electrode with various voltages on the auxiliary grid 1.5 mm from the 3-mm-thick field plate. Open symbols are for the 250-μm (0.010-in.) slit and solid symbols are for the 500-μm slit. Grid voltages are 0 V (circle), 500 V (triangle), and 1000 V (square), such that for the last two cases, the field direction is the same on both sides of the electrode. The calculated fields coincide for all three grid voltages with the small slit, but are distinguishable for the large one, with the greatest field shift occurring for 0 V on the grid. Measured values are adjusted to fit the calculations near the solid electrode. (The slit electrode is 7.2 mm from the solid plate.)

We conclude therefore that if the slit is well lapped and polished, the experimental configuration closely approaches the design geometry, and the spatial variation of the electrostatic field obtained from calculations and from field-mapping measurements corroborate each other. Accepting the computed field values, we can say that with the 250-μm-wide slit, the field deviates from the nominal value by 60 ppm at the surface of the plane electrode, and by about 500 ppm two-thirds of the distance to the mesh. As noted in Sec. VI C, the field varies essentially exponentially with the vertical distance. Between 1 and 2 mm from the plane electrode, the total field variation transverse to the atomic beam is less than 20 ppm. Since the longitudinal field variation can be reduced to a negligible value over a 1-cm decay length, we recommend the slot geometry for precision Stark spectroscopy.

VIII. CALIBRATION OF ELECTRIC FIELDS

The absolute calibration of electric fields to moderate accuracy is easily done by dividing the electrode spacing d into the potential difference V. However, the accuracy in the knowledge of the effective applied voltage is limited by contact potentials, imperfections on the electrode surfaces (e.g., patch effects), and possibly impurities deposited on the surfaces (e.g., charged dielectric contamination such as pump oil), while the accuracy of the spacing is limited by flatness and mechanical contacts as well as by deformations of the plates. Also, fringe field effects and the presence of other materials must be carefully accounted for in the calibration. The most accurate electric field primary calibration[40] used Stark effect observations with a molecular beam electric resonance apparatus and is quoted at 50 ppm, the uncertainty reported for the electric dipole moment of the OCS molecule. This primary standard is transferable by reference measurements on OCS.

One of the very important features of interference narrowing, as also the case for Stark energy level measurements in any simple atom, is that the absolute value of the field in principle is known *ab initio* to a high degree of accuracy by WKB QD Stark theory.[8–10] If the theory is sufficiently precise, the calculated field values will depend only on experimentally determined quantum-defect parameters and on the physical constants that provide a conversion from atomic to mks units. Such a calibration procedure would link electric field values directly to the atomic unit of field, which is presently known to better than 0.3 ppm.[41]

It is normally difficult to use Stark shifts for high-precision (<1000 ppm) field calibration because the shifts are not sufficiently large compared with typical probe laser line widths. Nevertheless, Stark energies near $n=40$ in He have recently been measured with a narrow band laser at fields near $F=260$ V/cm. The internal consistency of both the scale adjustments of these measurements and of the scatter of the data is in the order of 50 ppm.[42] Even though application of this approach to field calibration would require laser frequencies that are known absolutely to the order of 30 MHz, it is clearly worthy of further study. If the relevant energies can be calculated to this accuracy, a field calibration might be obtained.

Interference narrowing is ideally suited for calibration purposes because the narrow feature is highly localized in field. From a set of decay rate measurements over a narrowing region, the field at which the decay rate is minimum may be fit very precisely. At present, our data on individual narrowing regions are internally consistent to better than 15 ppm in some cases. However, there are discrepancies between different narrowings in rubidium on the order of 1000 ppm (0.1%). As this is far beyond the effects of uncertainties in the Rb quantum-defect values, we attribute these discrepancies to shortcomings of the semiclassical approximation used in the theory. More precise computational methods[43] are under study. We note that NMR is an accurate method for measuring magnetic fields, but until now there has been no counterpart for electric fields.

IX. CONCLUSIONS

We have exploited the interference narrowing of Stark resonances for the purpose of three-dimensional mapping of electric fields to an unprecedented level of precision. This is possible because of the very sharp field dependence of the width of these resonances in the vicinity of the narrowings. We have used this technique to detect effects of crinkles in a mesh electrode, machining imperfections in a slotted electrode, and slight lack of parallelness of electrode plates. When the geometry is sufficiently close to an ideal slotted electrode configuration, we are able to corroborate electrostatic field calculations for the field variation. By extending these calculations, we have presented the degree of field inhomgeneity as a function of the width of a slotted electrode. And finally, we have proposed a new method for absolute calibration of electric fields that has the potential for very high accuracy if present internal inconsistencies can be resolved by improvements in the theory.

ACKNOWLEDGMENTS

This work was supported by the National Science Foundation. Some of the electrostatic calculations were performed at the Cornell National Supercomputer Facility, a resource of the Center for Theory and Simulation in Science and Engineering (Cornell Theory Center). We are indebted to D. Harmin for subroutines used to compute Stark energy levels and widths, and to J. Kycia for help running the programs.

---

[*] Present address: Radio-Electronics Department, Peking University, Beijing 100 871, China.

[1] S. Feneuille, S. Liberman, E. Luc-Koenig, J. Pinard, and A. Taleb, J. Phys. B **15**, 1205 (1982).

[2] J.-Y. Liu, *et al.*, Phys. Rev. Lett. **55**, 189 (1985).

[3] P. McNicholl *et al.*, Phys. Rev. A **37**, 3302 (1988).

[4] C. Chardonnet, D. Delande, and J. C. Gay, Phys. Rev. A **39**, 1066 (1988).

[5] D.-H. Yang *et al.*, Bull. Am. Phys. Soc. **33**, 933 (1988).

[6] A. Nussenzweig, C. Cornaggia, E. E. Eyler, T. Bergeman, and E. Pollack, in Abstracts of the Eleventh International Conference on Atomic Physics, Paris, 1988.

[7] A. König and H. Rinneberg (private communication).

[8] D. A. Harmin, Phys. Rev. A **24**, 2491 (1981).

[9] D. A. Harmin, Phys. Rev. A **26**, 2656 (1982).

[10] D. A. Harmin, Phys. Rev. A **30**, 2413 (1984).

[11] I. Langmuir, J. Franklin Inst. **196**, 751 (1923).

[12] E. Weber, *Electromagnetic Theory* (Dover, New York, 1965).

[13] I. Nemirovsky and N. Freschki, J. Phys. B **15**, 2579 (1982).

[14] Y. Hamasaki *et al.*, Electron-Lett. **16**, 406 (1980).

[15] S. R. M. Robertson and A. J. Rogers, IEEE Proc. J. **132**, 195 (1985).

[16] K. Koo and G. Sigel, IEEE J. Quantum Electron **QE-18**, 670 (1982).

[17] D. Doughty and J. Lawler, Appl. Phys. Lett. **45**, 611 (1984).

[18] B. N. Ganguly and A. Garscadden, Phys. Rev. A **32**, 2544 (1985).

[19] D. K. Doughty, S. Salih, and J. E. Lawler, Phys. Lett. **103A**, 41 (1984).

[20] C. A Moore, G. P. Davis, and R. A. Gottscho, Phys. Rev. Lett. **52**, 538 (1984).

[21] J. Derouard and N. Sadeghi, IEEE Trans. Plasma Sci. **PS14**, 515 (1986).

[22] M. L. Zimmerman, M. G. Littman, M. M. Kash, and D. Kleppner, Phys. Rev. A **20**, 2251 (1979).

[23] K. Sakimoto, J. Phys. B **19**, 3011 (1986).

[24] P. McNicholl and H. J. Metcalf, Appl. Opt. **24**, 2757 (1985).

[25] P. McNicholl, Ph.D. thesis, State University of New York at Stony Brook, New York, 1986 (unpublished).

[26] When we are not concerned about preserving the time dependence of the signal, we place a 1-kΩ resistor on this line for convenience.

[27] L. Lapidus and G. F. Pinder, *Numerical Solution of Partial Differential Equations in Science and Engineering* (Wiley, New York, 1982).

[28] C. W. Steele, *Numerical Computation of Electric and Magnetic Fields* (Van Nostrand Reinhold, New York, 1987).

[29] K. Halbach, Nucl. Instrum. Methods **64**, 278 (1968); K. Halbach and R. F. Holsinger, Part. Accel. **7**, 213 (1976). The POISSON codes are available from group AT-6, Los Alamos National Laboratory. Our use of these codes was made possible by H. Kirk of Brookhaven National Laboratory and by L. Moorman of State University of New York at Stony Brook.

[30] For example, the ANSYS–PC/THERMAL programs available from Swanson Analysis Systems, Inc. Houston, PA may be used for the Laplace equation in three dimensions.

[31] H. Schwarz, J. Reine Angew. Math. **70**, 105, (1869).

[32] R. Courant and D. Hilbert, *Methods of Mathematical Physics* (Wiley Interscience, New York, 1962), Vol. II.

[33] *First International Symposium on Domain Decomposition Methods for Partial Differential Equations,* edited by R. Glowinski, G. H. Golub, G. A. Meurant, and J. Periaux (SIAM, Philadelphia, 1988).

[34] W. P. Tang, Ph.D. thesis, Stanford University, Stanford, California 1987 (unpublished). We are indebted to T. Hagstrom for directing us to this work.

[35] P. M. Morse and H. Feshbach, *Methods of Theoretical Physics* (McGraw-Hill, New York, 1953).

[36] J. D. Jackson, *Classical Electrodynamics,* 2nd ed. (Wiley, New York, 1975), Chap. 3.

[37] J. L. Verster, Philips Res. Rep. **18**, 465 (1963). We are indebted to Michael Scheinfein of the National Institute of Standards and Technology for this reference.

[38] Mesh obtained from Buckbee Mears Co., Minneapolis, MN.

[39] We used cyanoacrylate or silver acrylate (Dupont No. 4922) glue.

[40] F. H. De Leeuw and A. Dymanus, Chem. Phys. Lett. **7**, 288 (1970); J. Reinartz and A. Dymanus, *ibid.*, **24**, 346 (1974).

[41] This estimate is obtained with the fundamental constants given by E. R. Cohen and B. N. Taylor, Rev. Mod. Phys. **59**, 1121 (1987) using the definition of atomic units in H. A. Bethe and E. E. Salpeter, *Quantum Mechanics of One- and Two-Electron Atoms* (Springer, Berlin, 1957).

[42] A. Nussenzweig, E. E. Eyler, T. Bergeman, and E. Pollack (private communication).

[43] F. Robicheaux, U. Fano, M. Cavagnero, and D. Harmin, Phys. Rev. **35**, 3619 (1987).